




## Article

# Analysis of Wave Breaking on Gaofen-3 and TerraSAR-X SAR Image and Its Effect on Wave Retrieval

Ruozhu Zhong<sup>1</sup>, Weizeng Shao<sup>1,2,3,\*</sup> , Chi Zhao<sup>1</sup>, Xingwei Jiang<sup>2,3</sup> and Juncheng Zuo<sup>1</sup><sup>1</sup> College of Marine Sciences, Shanghai Ocean University, Shanghai 201306, China<sup>2</sup> National Satellite Ocean Application Service, Ministry of Natural Resources, Beijing 100081, China<sup>3</sup> Southern Marine Science and Engineering Guangdong Laboratory (Guangzhou), Guangzhou 511458, China

\* Correspondence: wzshao@shou.edu.cn; Tel.: +86-216-190-0326

**Abstract:** The main purpose of our work is to investigate the performance of wave breaking and its effect on wave retrieval in data acquired from the Chinese Gaofen-3 (GF-3) synthetic aperture radar (SAR) at C-band and the German TerraSAR-X (TS-X) at X-band. The SAR images available for this study included 140 GF-3 images acquired in quad-polarization strip (QPS) mode and 50 dual-polarized (vertical-vertical (VV) and horizontal-horizontal (HH)) TS-X images acquired in stripmap (SM) mode. Moreover, these images were collocated with the waves simulated by the numeric WAVEWATCH-III (WW3) (version 5.16) model and HYbrid Coordinate Ocean Model (HYCOM) current. In particular, a few images covered the moored buoys monitored by the National Data Buoy Center (NDBC) of the National Oceanic and Atmospheric Administration (NOAA). The comparison between the WW3-simulated results and the significant wave heights (SWHs) from the European Centre for Medium-Range Weather Forecasts (ECMWF) reanalysis data (ERA-5) showed that the correlation coefficient (COR) was 0.4–0.6 with a root mean squared error (RMSE) of about 0.2 m at SWHs of 0–4 m. The winds were inverted using VV-polarized geophysical model functions (GMFs), e.g., CSARMOD-GF for the GF-3 images and XMOD2 for the TS-X images. The Bragg resonant roughness in the normalized radar cross section (NRCS) was simulated using a radar backscattering model and the SAR-derived wind, WW3-simulated wave parameters, and HYCOM current. Then, the contribution of the non-polarized (NP) wave breaking to the SAR data was estimated by the VV-polarized NRCS, the HH-polarized NRCS, and the polarization ratio (PR) of the co-polarized Bragg resonant components in the NRCS. Because co-polarized Bragg resonant components in the NRCSs have poor results, due to the saturation for wind speeds greater than 20 m/s, the analysis of wave breaking is excluded at such conditions. The results revealed that the backscattering signal in the C-band was more sensitive to wave breaking than the backscattering signal in the X-band. Interestingly, the ratio had a linear correlation with wind speed. Moreover, the variation in the bias (inverted SWH minus WW3 simulation) showed that the bias increased as the wind speed (>8 m/s) and whitecap coverage (>0.005) increased. Following this rationale, wave retrieval during tropical cyclones should consider the influence of wave breaking.



**Citation:** Zhong, R.; Shao, W.; Zhao, C.; Jiang, X.; Zuo, J. Analysis of Wave Breaking on Gaofen-3 and TerraSAR-X SAR Image and Its Effect on Wave Retrieval. *Remote Sens.* **2023**, *15*, 574. <https://doi.org/10.3390/rs15030574>

Academic Editor: Antonio Iodice

Received: 7 December 2022

Revised: 12 January 2023

Accepted: 14 January 2023

Published: 18 January 2023

**Keywords:** wave breaking; Gaofen-3; TerraSAR-X

**Copyright:** © 2023 by the authors. Licensee MDPI, Basel, Switzerland. This article is an open access article distributed under the terms and conditions of the Creative Commons Attribution (CC BY) license (<https://creativecommons.org/licenses/by/4.0/>).

## 1. Introduction

Sea surface waves are essential in oceanographic dynamics and affect the energy exchange at the air-sea interface [1]. When waves propagate from the open sea to coastal waters, wave breaking occurs due to the rapid change in wave height. This type of small-scale wave breaking (~1 km) is usually measured by moored buoys in coastal waters. However, the spatial resolution of moored buoy data cannot satisfy the requirements for oceanographic research, especially for research on tropical cyclones [2] and open sea areas [3]. Utilizing remote sensing technology, the dynamics at the sea surface layer have been detected by passive satellites operating in the microwave band [4]. Typically,

sea surface winds are derived from scatterometer data [5] having a spatial resolution of up to gridded 15 km, and waves are derived from altimeter data following the 10 km footprints [6]. Synthetic aperture radar (SAR) is an active sensor for detecting information about the sea surface with a fine spatial resolution and large coverage, e.g., a pixel size of 8 m for the C-band Gaofen-3 (GF-3) synthetic aperture radar (SAR) acquired in quad-polarized strip mode (QPS) [7,8] and a pixel size of 3 m for the X-band dual-polarized TerraSAR-X (TS-X) acquired in stripmap mode (SM) [9]. Traditionally, the sea surface winds and waves are two parameters that are measured simultaneously by SAR, and they are closely related to wave breaking. Therefore, SAR-derived winds and waves are valuable for wave breaking detection.

Till now, algorithms for wind retrieval on SAR have been adopted for various SAR sensors [10]. The basic principle is that the backscattering signal, called the normalized radar cross section (NRCS), is directly related to a wind vector and radar incidence angle [11]. In the application to SAR wind retrieval, a geophysical model function (GMF) is designed in the co-polarization channel (vertical-vertical (VV) and horizontal-horizontal (HH)), e.g., the CMOD at C-band [7,8], XMOD at X-band [12], and LMOD at L-band [13]. According to [14–16], the accuracy of the wind speed obtained using a GMF is 2 m/s based on validation against other remote sensing products and measurements of moored buoys at low-to-moderate wind speeds. When the wind speed exceeds 25 m/s, the SAR backscattering signal tends to saturate [17], and the GMF is not applicable for wind retrieval under such conditions. The high wind speeds in tropical cyclones can be retrieved from SAR images in the cross-polarization (vertical-horizontal (VH) and horizontal-vertical (HV)) channels [18,19] because the SAR-measured NRCS becomes saturated at wind speeds >50 m/s.

The sea surface wave mapping mechanism of SAR includes three modulations, e.g., tilt modulation [20], hydrodynamic modulation [21], and non-linear velocity bunching [22,23]. The first wave retrieval algorithm, called the Max Planck Institute algorithm (MPI) [24], is based on spectral transformations and takes the numerical-model simulated waves as the inputs in order to simulate the SAR intensity spectrum using the modulation transfer function (MTF) of each SAR mapping modulation. Then, it retrieves the ocean wave spectrum by minimizing a cost function between the simulated and observed SAR intensity spectra. Several algorithms have been developed, such as the semi-parametric retrieval algorithm (SPRA) [25], the partition rescaling and shift algorithm (PARSA) [26], and the parameterized first-guess spectrum method (PFSM) [27]. In addition, empirical models have been designed to directly estimate the wave parameters, e.g., the CWAVE model [28] at C-band and the XWAVE model at X-band [29], because a few SAR acquisitions can be implemented via spectral transformations for wave retrieval, e.g., 30% or acquisitions for Sentinel-1 interferometric wide swath mode [30]. Although the accuracy of SAR-derived waves is about 0.6 m [12], the existing wave retrieval algorithms do not consider the wave breaking term in their schemes.

In fact, wave breaking has an effect on SAR wind retrieval [17]. The spatial scale of the wind on SAR is about 3 km [31], called the wind streak [32], and the non-polarized (NP) contribution on the SAR NRCS caused by wave breaking is supposedly related to the sea surface wind speed [33,34]. Utilizing quad-polarized RADARSAT-2 (R-2) SAR images, an empirical model for NP estimation has recently been developed [35] without considering the sea state and radar frequency. In a recent study [36], it was revealed that the NP empirical model has to be adopted for Chinese Gaofen-3 SAR images. Moreover, wave breaking can distort the SAR intensity spectrum, causing an error in the theoretical-based wave retrieval scheme. The wave breaking term is also not included in the existing empirical models for SAR wave retrieval. In this study, a theoretical-based method [37] was used to estimate the NP contribution in NRCS using the dual-polarized (VV and HH) backscattering signals. The main purpose of our work is to investigate the performance of wave breaking in dual-polarized C-band GF-3 and X-band TerraSAR-X (TS-X) data in term of various sea state, e.g., wind speed, SWH and current. The NP wave breaking in a small

scale has influence on the homogeneity of the SAR image. In this sense, the effect of wave breaking on wave retrieval using the PFSM algorithm was also studied.

The remainder of this study is organized as follows. Section 2 introduces the available datasets, e.g., SAR images, sea surface wind from the European Centre for Medium-Range Weather Forecasts (ECMWF) reanalysis data (ERA-5), sea surface current from the HYbrid Coordinate Ocean Model (HYCOM), the measurements from National Data Buoy Center (NDBC) buoys, and the settings of the WAVEWATCH-III (WW3) (latest version 6.07) model. The methodology of NP estimation, the backscattering model for the SAR surface, and the scheme of SAR wave retrieval (i.e., the PFSM) are described in Section 3. The results and discussion are given in Sections 4 and 5 summarizes the conclusions.

## 2. Datasets

### 2.1. SAR Images and In Situ Data

In total, 140 GF-3 images acquired in QPS mode and 50 dual-polarized TS-X images acquired in stripmap (SM) mode were used for analysis. In particular, a few images covered the moored buoys of the NDBC of the National Oceanic and Atmospheric Administration (NOAA). The calibration method for inverting the GF-3 and TS-X intensities into an NRCS has been described in a previous study [8] and the document can be obtained at <https://www.intelligence-airbusds.com/files/pmedia/public> (accessed on 1 January 2023). Therefore, the process is not described here. As examples, a calibrated ( $128 \times 128$  pixels) VV-polarized GF-3 SAR image acquired at 1:58 UTC on 5 May 2017, and a TS-X image acquired at 16:53 UTC on 3 August 2009, are shown in Figure 1a,b, respectively. Note that the white crosses represent the geographic locations of three moored buoys (IDs: 46054, 51001, and 51101).

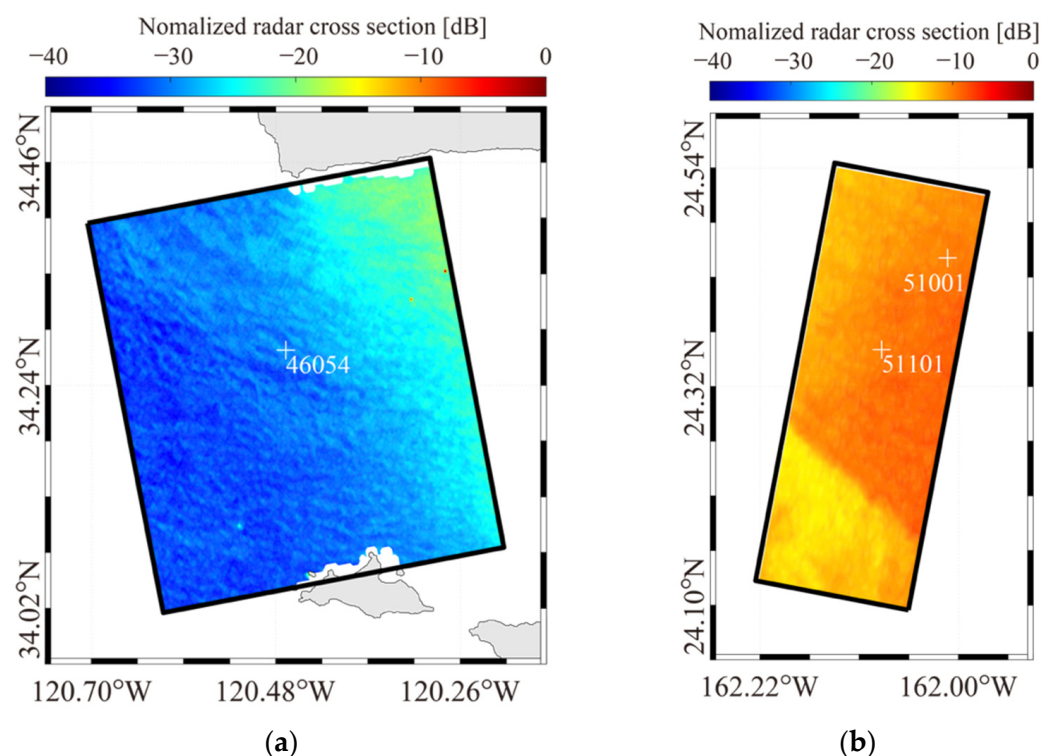


**Figure 1.** Synthetic aperture radar (SAR) measured normalized radar cross sections (NRCSs) of (a) a VV-polarized Gaofen-3 (GF-3) image acquired at 01:58 UTC on 5 May 2017 and (b) a TerraSAR-X (TS-X) image acquired at 16:53 UTC on 3 August 2009. Note that the three buoys located in these images are marked by white crosses.

## 2.2. Hindcast Data

Although the real-time measurements from buoys are accurate resources for studying the influence of wave breaking on SAR wave retrieval, a third-generation numerical model was more useful due to its wide spatial coverage and fine resolution. At present, two well-known models, namely, the WW3 model and simulating waves nearshore (SWAN) model, are well-designed for wave simulation [3]. The SWAN model works on unstructured grids, indicating that it has good performance in coastal waters, while the WW3 model usually operates on structured grids. Because all the SAR images were located in the open sea, the WW3 model was chosen as the most suitable model for the wave simulation.

The forcing field was the ERA-5 winds on a grid of  $0.25^\circ$  at an interval of 1-h, and the bathymetric topography was the water depth from the General Bathymetric Chart of the Oceans (GEBCO) on a grid of 1 km in the horizontal direction. As was mentioned by Hu et al. [38], the performance of the model-simulated waves could be improved when the sea surface current is included. The sea surface current field with a  $0.08^\circ$  grid at an interval of 3 h collected from the official HYCOM datasets was also treated as a forcing field. The outputs of the WW3 model included the significant wave height (SWH) and the whitecap coverage, both of which have the same spatial resolution of 1 km at an interval of 30-min. The details of the model settings are listed in Appendix A. The wind maps from the ERA-5 data collected at 2:00 UTC on 5 May 2017 and at 17:00 UTC on 3 August 2009 are presented in Figure 2a,b, respectively. Note that the rectangles denote the spatial coverages of the two images in Figure 1. It is observed that the  $0.25^\circ$  gridded ERA-5 wind profile has a significant gradient ( $\sim 8$  m/s) on both sides of the GF-3 image, which causes the nearly 20-dB difference for around  $50 \times 50$  km coverage in Figure 1a. Similarly, the maps of the sea surface current fields from HYCOM at 3:00 UTC on 5 May 2017 and at 18:00 UTC on 3 August 2009 are shown in Figure 3a,b, respectively.

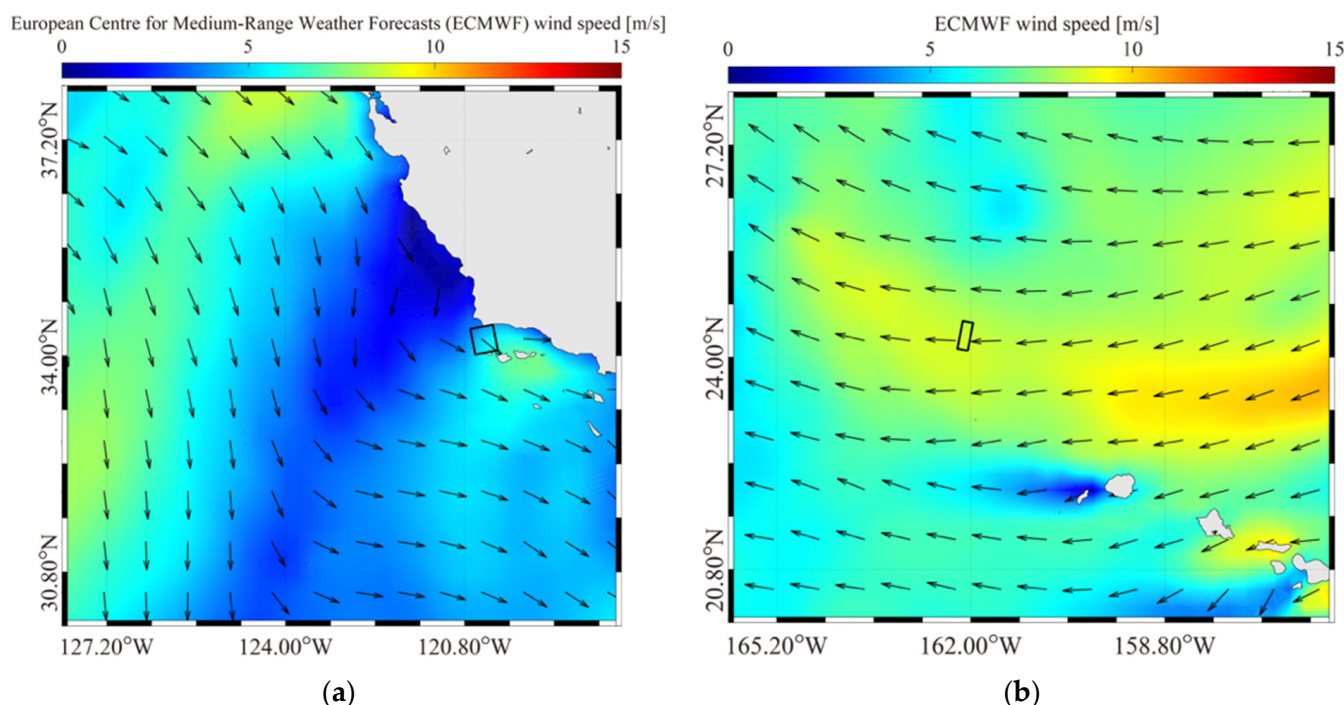


**Figure 2.** (a) The European Centre for Medium-Range Weather Forecasts (ECMWF) reanalysis data (ERA-5) wind map at 2:00 UTC on 5 May 2017; and (b) The ERA-5 wind map at 17:00 UTC on 3 August 2009. The black rectangle denotes the spatial coverage of two images in Figure 1.

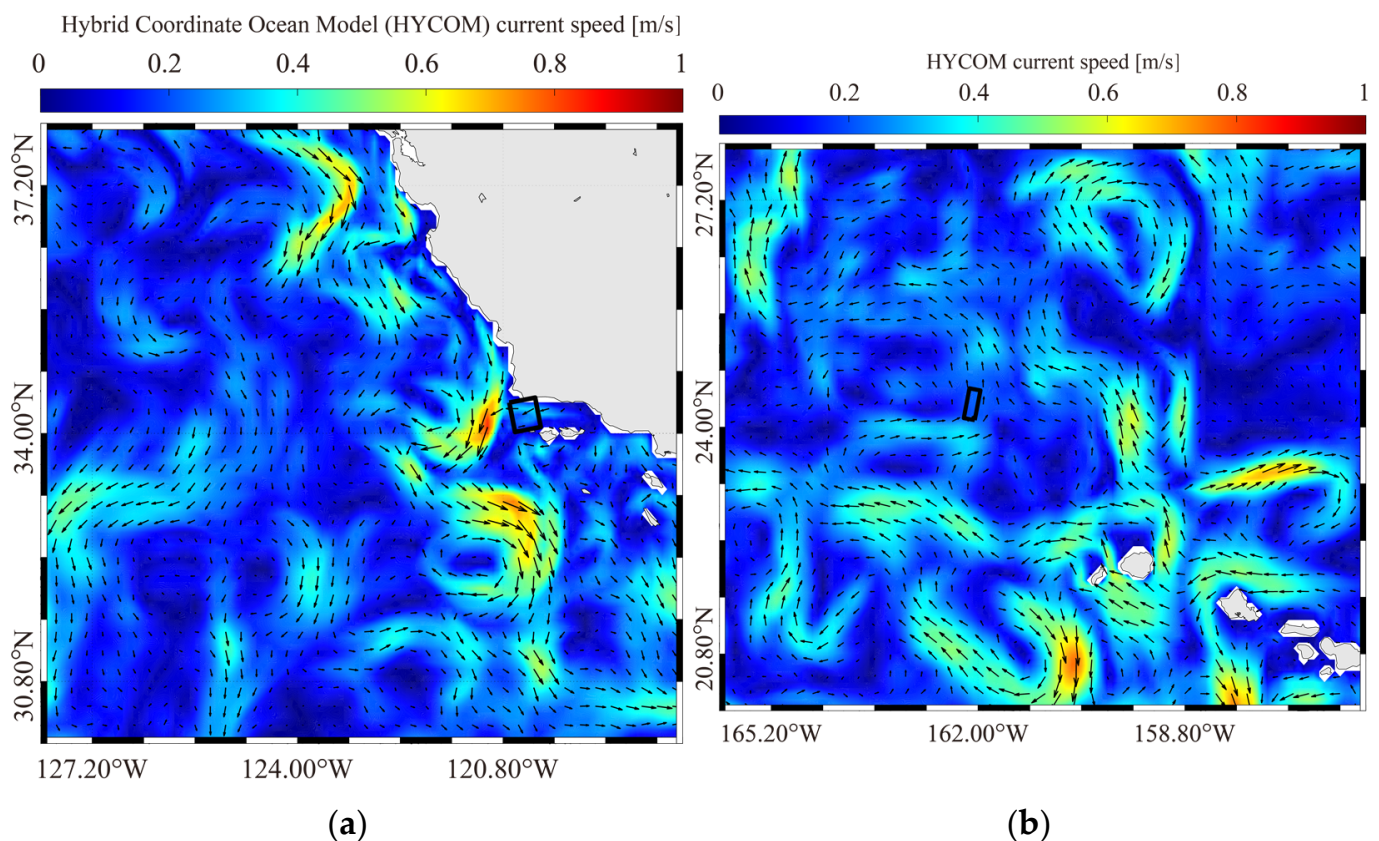


**Figure 3.** (a) The HYbrid Coordinate Ocean Model (HYCOM) sea surface current map at 3:00 UTC on 5 May 2017; and (b) The HYCOM sea surface current map at 18:00 UTC on 3 August 2009. The black rectangle denotes the spatial coverage of two images in Figure 1.

The SWH data from the ERA-5 were directly employed so as to validate the simulation results from the WW3 model. Moreover, the model-simulated whitecap coverage was also compared with the results calculated using the wind and wave data from NDBC buoys. For instance, the SWH cases from the ERA-5 and WW3 model are shown in Figure 4a,b, respectively. It can be seen that the ERA-5 SWHs have gaps in the coastal waters due to the coarse spatial resolution. The calculation formulas are described in Appendix B. Using a Taylor diagram, the WW3-simulated SWH was validated against the ERA-5 and the WW3-simulated whitecap coverage was validated against the NDBC buoy data (Figure 5a,b, respectively). It was found that the correlation coefficient (COR) of the SWHs of the WW3-simulated and ERA-5 was 0.4–0.6 with a root mean squared error (RMSE) of about 0.2 m for SWHs of 0–4 m. The ERA-5 data is a reanalysis dataset assimilated by various observations from buoys and satellite products. That is why the COR is not significant, the ERA-5 data could not simultaneously provide the whitecap coverage. The COR of the whitecap coverage was about 0.4 and the RMSE was 0.1–0.3; however, the COR reached 0.6 at wind speeds of 15–18 m/s.

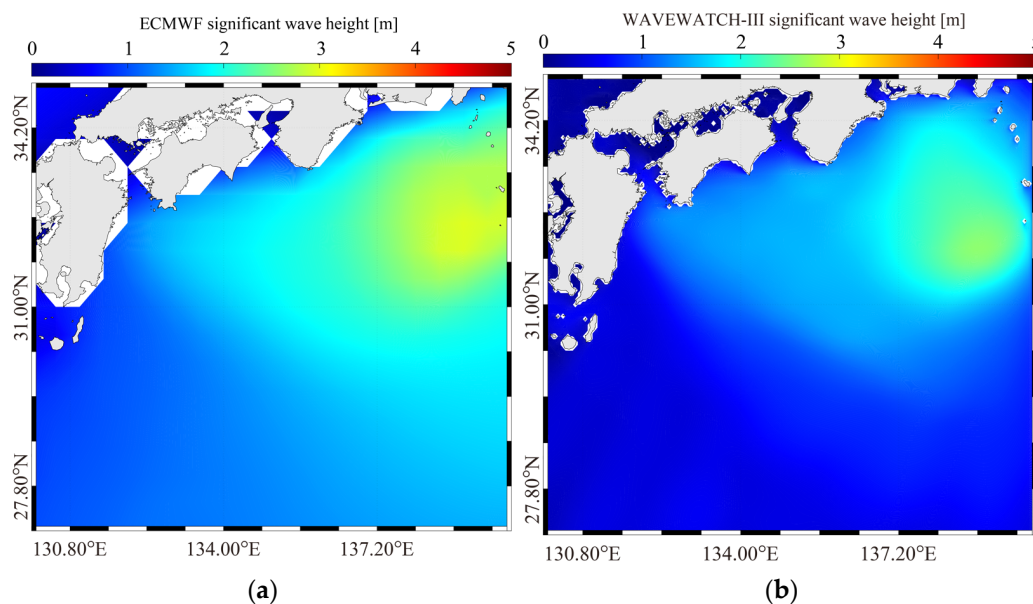


**Figure 4.** The significant wave height (SWH) maps at 09:00 UTC on 20 Sep 2021 from the (a) ERA-5 and (b) WAVEWATCH-III (WW3) data.

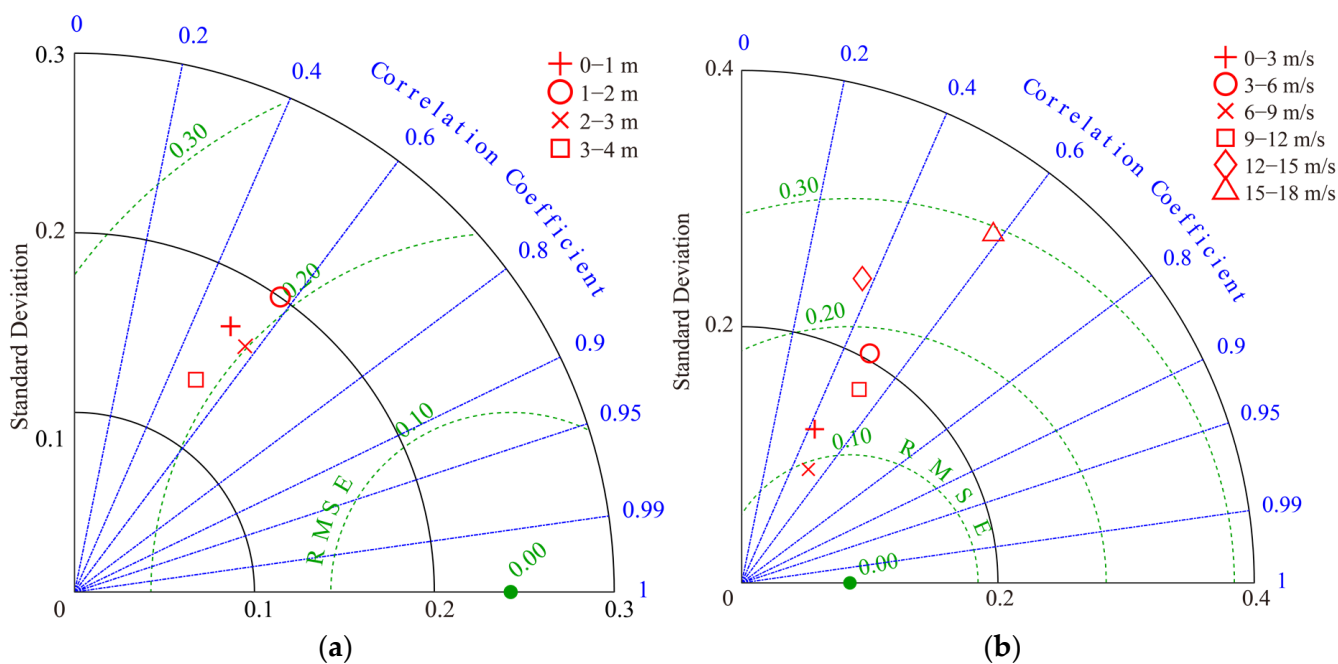


**Figure 5.** (a) Validation of WW3-simulated SWHs against ERA-5 for SWHs of 0–4 m; and (b) validation of WW3-simulated whitecap coverage against NDBC buoy data at wind speeds 0–18 m/s.

### 3. Methodology

In order to investigate the performance of wave breaking on C- and X-band SAR, which is useful for the improvement of SAR wave retrieval, the estimation of NP is essential for this study. Therefore, the theoretical approach for NP estimation [37] is briefly described, in which the Bragg backscattering model is introduced to calculate the resonant component in NRCS at moderate incidence angles [39,40]. Additionally, the wave retrieval algorithm PFSM is briefly presented.

### 3.1. NP Estimation

According to the microwave radar imaging mechanism, the radar instrument receives electromagnetic energy determined by the geometric distributions on the sea surface, which depends quantitatively on microwave waves backscattered by the gravity-capillary waves (Bragg waves). Additionally, the reflection in the specular direction and NP component induced by wave breaking also modulate the sea surface roughness. Following this rationale, the NRCS  $\sigma_0$  can be written as

$$\sigma_0 = \sigma_{br} + \sigma_{sp} + \sigma_{wb} \quad (1)$$

in which  $\sigma_{br}$  is the resonant component of the Bragg backscattering,  $\sigma_{sp}$  is the term associated with the specular reflection, and  $\sigma_{wb}$  is the contribution of the NP wave breaking. It should be noted that the specular reflection term  $\sigma_{sp}$  has little contribution at incidence angles of 20–50° [41]. Therefore, the NP component is directly removed by the polarization difference  $\Delta\sigma_0$  (the VV-polarized  $\sigma_0^{VV}$  minus the HH-polarized  $\sigma_0^{HH}$ ):

$$\Delta\sigma_0 = \sigma_0^{VV} - \sigma_0^{HH}, \quad (2)$$

in which the polarization difference  $\Delta\sigma_0$  is independent of the NP and the specular reflection because both are not polarization selective.

By substituting Equation (2) into Equation (1), the NP component  $\sigma_{wb}$  can be related to  $\Delta\sigma_0$  and the polarization ratio PR between the VV-polarized  $\sigma_{br}^{VV}$  and HH-polarized  $\sigma_{br}^{HH}$  resonant component of the Bragg backscattering:

$$\sigma_{wb} = \sigma_0^{VV} - \frac{\Delta\sigma_0}{1 - PR} \quad (3)$$

$$PR = \frac{\sigma_{br}^{VV}}{\sigma_{br}^{HH}} \quad (4)$$

In summary, the contribution of the  $\sigma_{wb}$  can be calculated from the  $\sigma_0^{VV}$ ,  $\sigma_0^{HH}$ , and PR of the Bragg resonant component in the co-polarization channel. As mentioned in [37], the PR is empirically derived using wave parameters associated with wind speed, however, this approach is practically applied for fully-developed sea states as taking advantage of Pierson–Moskowitz wave spectrum [42,43]. In this study, the Bragg resonant in NRCS is simulated according to backscattering theory, in which the complicated modulation of sea surface current is considered.

### 3.2. Radar Backscattering Model

As mentioned in Equation (1), SAR backscattering includes Bragg backscattering and wave breaking contributions. Equation (12) is used to obtain the Bragg resonant roughness NRCS  $\sigma_{br}$  in the VV and HH channel, which is based on the theoretical rationale proposed by Romeiser et al. [44]:

$$\sigma_{br} = \frac{\iint \sigma dx dy}{xy}, \quad (5)$$

in which  $\sigma$  is the backscattering cross section (RCS); and the dimensions  $x$  and  $y$  denote the horizontal and vertical dimensions, respectively. The RCS is proportional to the wave energy spectrum  $E$  produced using the parametric function derived by Elfouhaily et al. [45]:

$$\sigma = wB_s E(k_{br}, \phi_{br}), \quad (6)$$

where

$$k_{br} = 2k_0 \sqrt{\sin^2(\theta - S_p) + \cos^2(\theta - S_p) \sin^2(S_t)} \quad (7)$$

$$\phi_{br} = \phi + \tan^{-1} \frac{\cos(\theta - S_p) \sin(-S_t)}{\sin(\theta - S_p)} \quad (8)$$

$$w = \frac{\cos(\theta - S_p)}{\cos \theta \times \cos S_p}. \quad (9)$$

In Equations (6)–(8),  $k_{br}$  and  $\phi_{br}$  are the wave number and propagation direction of the Bragg wave number (Equations (7) and (8), respectively);  $w$  is the weighting function (Equation (9));  $k_0$  is the wave number of microwave radar (i.e., ~5 cm for GF-3 and 3 cm for TS-X);  $\theta$  is the radar incidence angle;  $\phi$  is the satellite's flight direction; and  $S_p$  and  $S_t$  are the Bragg wave-tilted slopes parallel and normal to the direction of the radar beam.  $B_s$  is the Bragg scattering coefficient, which is evaluated as follows:

$$B_s = 8\pi k_0^4 \cos^4 \theta_i \left| \left( \frac{\sin(\theta - S_p) \cos S_t}{\sin \theta_i} \right)^2 b_{HH} + \left( \frac{\sin S_t}{\sin \theta_i} \right)^2 b_{VV} \right|^2, \quad (10)$$

where

$$\theta_i = \cos^{-1}(\cos(\theta - S_p) \times \cos S_t), \quad (11)$$

$$S_p = \tan^{-1}\left(\cos \phi \frac{\partial \zeta}{\partial x} + \sin \phi \frac{\partial \zeta}{\partial y}\right), \quad (12)$$

$$S_t = \tan^{-1}\left(-\sin \phi \frac{\partial \zeta}{\partial x} + \cos \phi \frac{\partial \zeta}{\partial y}\right) \quad (13)$$

$$b_{HH} = \frac{\varepsilon}{(\cos \theta_i + \sqrt{\varepsilon})^2} \quad (14)$$

$$b_{VV} = \frac{\varepsilon^2(1 + \sin^2 \theta_i)}{(\varepsilon \cos \theta_i + \sqrt{\varepsilon})^2}. \quad (15)$$

In Equations (10)–(15),  $\varepsilon$  is the permittivity of seawater,  $\theta_i$  is the effective incidence angle, and  $\zeta$  is the sea surface height modulated by the wave and current fields.

In summary, several variables are needed to obtain the Bragg resonant roughness  $\sigma_{br}$ , including the incidence angle  $\theta$ , flight direction  $\phi$ , and wind speed at 10-m height  $U_{10}$ , to produce the wave spectrum  $E$  using the well-known wind-sea Joint North Sea Wave Project (JONSWAP) model [46], and to forward calculate the sea surface slopes together with the current. As revealed in [17], the co-polarized NRCS suffers saturation problems at high winds (i.e., >25 m/s), and the simulated Bragg resonant component in NRCS has poor results at such conditions.

### 3.3. Wave Retrieval Algorithm

In recent decades, SAR wave retrieval algorithms have been well studied. In our recent studies [47,48], it was proved that the PFSM algorithm is applicable for wave retrieval from GF-3 and TS-X images. Therefore, the SAR-derived waves were obtained from the collected GF-3 and TS-X images using the PFSM algorithm. It should be noted that wind retrieval was necessary for conducting SAR wave retrieval. The CSARMOD-GF [8] and XMOD2 [12] GMFs were used for the GF-3 and TS-X wind retrieval, respectively.

The scheme of the PFSM algorithm follows the principle of the MPI algorithm. Specifically, the key is to minimize the cost function  $J$ :

$$J = \int [F_k - \bar{F}_k]^2 dk + \mu \int \left\{ \frac{[S_k - \bar{S}_k]}{[B + \bar{S}_k]} \right\}^2 dk \quad (16)$$

where  $F_k$  is the first-guess spectrum produced by the JONSWAP model;  $\bar{F}_k$  is the SAR-derived wave spectrum obtained in the minimization process;  $\bar{S}_k$  is the mapping SAR spectrum obtained using the wave spectrum;  $S_k$  is the SAR original intensity spectrum;  $\mu$  is the weight coefficient; and  $k$  is the wave number. The constant  $B$  is assumed to be 0.001 so as to ensure convergence of the iteration.



In fact, the SAR intensity spectrum could be divided into two portions: linear and nonlinear components. The wave spectrum is inverted by the corresponding SAR spectrum. The unique improvement of the PFSM algorithm is the calculation of the threshold wave number  $k_s$ , which is employed for the division of the SAR intensity spectrum into a linear-mapped wind portion and a nonlinear-mapped swell portion [49]:

$$k_s = \left( \frac{2.87gV^2}{R^2 U_{10}^4 \cos^2 \varphi (\sin^2 \varphi \sin^2 \theta + \cos^2 \varphi)} \right)^{0.33}, \quad (17)$$

in which  $g = 9.8 \text{ m/s}^2$ ;  $V = 7600 \text{ m/s}$ ;  $R$  is the distance in the slant direction;  $U_{10}$  is the wind speed;  $\theta$  is the incidence angle; and  $\varphi$  is the angle of the wave propagation direction relative to the direction of the radar beam.

Regarding the nonlinear mapped SAR intensity spectrum, in which the wave number  $k$  is greater than  $k_s$ , the wave spectrum is initially produced by the JONSWAP, which is treated as a first-guess spectrum in Equation (16), and then, the wind-sea spectrum is inverted from the corresponding SAR portion after minimizing the cost function  $J$ . The swell spectrum is simply inverted from the linear-mapped SAR portion, in which the wave number  $k$  is less than  $k_s$ , without considering the non-linear velocity bunching modulation. It was found that the RMSE of the SWH was about 0.5 m when using the PFSM algorithm for GF-3 [47] and TS-X [46] SAR images.

The overall workflow of this study is illustrated in Figure 6.

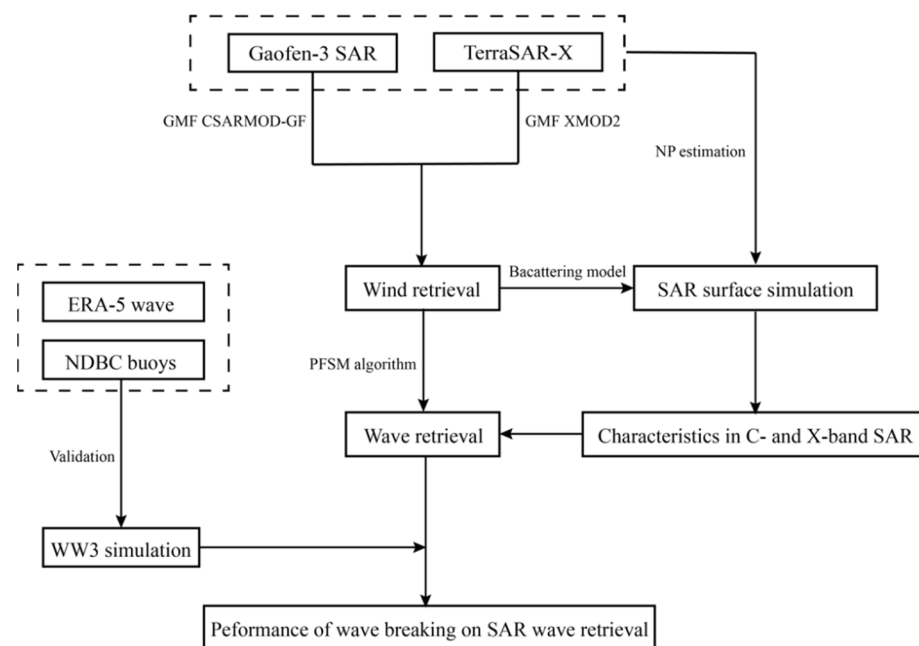


**Figure 6.** Flowchart of the study of the performance of wave breaking on SAR wave retrieval.

#### 4. Results and Discussion

In this section, a case is presented in order to illustrate the wind speed map from GF-3 and TS-X images. First, the inverted one-dimensional wave spectrum is presented, and then, the SWH retrievals are systematically compared with the SWHs from the WW3 model. Furthermore, the applicability of the NRCS to the difference in dual-polarized C-band and X-band (the composited simulation including the Bragg resonant and the N-P contribution minus the SAR-measured NRCS) in terms of the various dynamic parameters, e.g., the inverted wind speed from SAR image, HYCOM sea surface current, and inverted SWH from SAR image, is analyzed.

#### 4.1. Wind and Wave Retrieval

The wind speeds from GF-3 and TS-X images having about 1 km spatial resolution were retrieved using prior information about the ERA-5 wind directions. Figure 7 shows the SAR-derived wind maps by the VV-polarized GMF CSARMOD-GF and XMOD2. The accuracy of the wind retrieval has been well-studied when validating the SAR-derived results against buoy and scatterometer data, e.g., RMSEs of 1.8 m/s and 1.5 m/s for GF-3 [8] and TS-X [12], respectively. Therefore, the validation of the retrieval wind speeds is not repeated in this study. Figure 8a,b show the one-dimensional wave spectra obtained using the PFSM scheme from the sub-scene on the GF-3 SAR image covering a buoyed area (ID: 46054) and the sub-scene on the TS-X image covering a buoyed area (ID: 51001), respectively. The retrieval results for all of the sub-scenes derived from the GF-3 and TS-X images were compared with the simulations from the WW3 model. Statistical analysis of the SAR-derived SWH was conducted using the Taylor diagram in terms of the SAR-derived wind speed (Figure 9). It was found that the RMSE of the SWH was about 0.5 m and the COR was  $>0.8$ . Moreover, the accuracy was slightly reduced ( $\text{RMSE} > 0.4$  m) at low and high wind speeds ( $<5$  m/s and  $>20$  m/s). This result is consistent with the conclusions of several studies conducted on SAR wave retrieval [30,46].

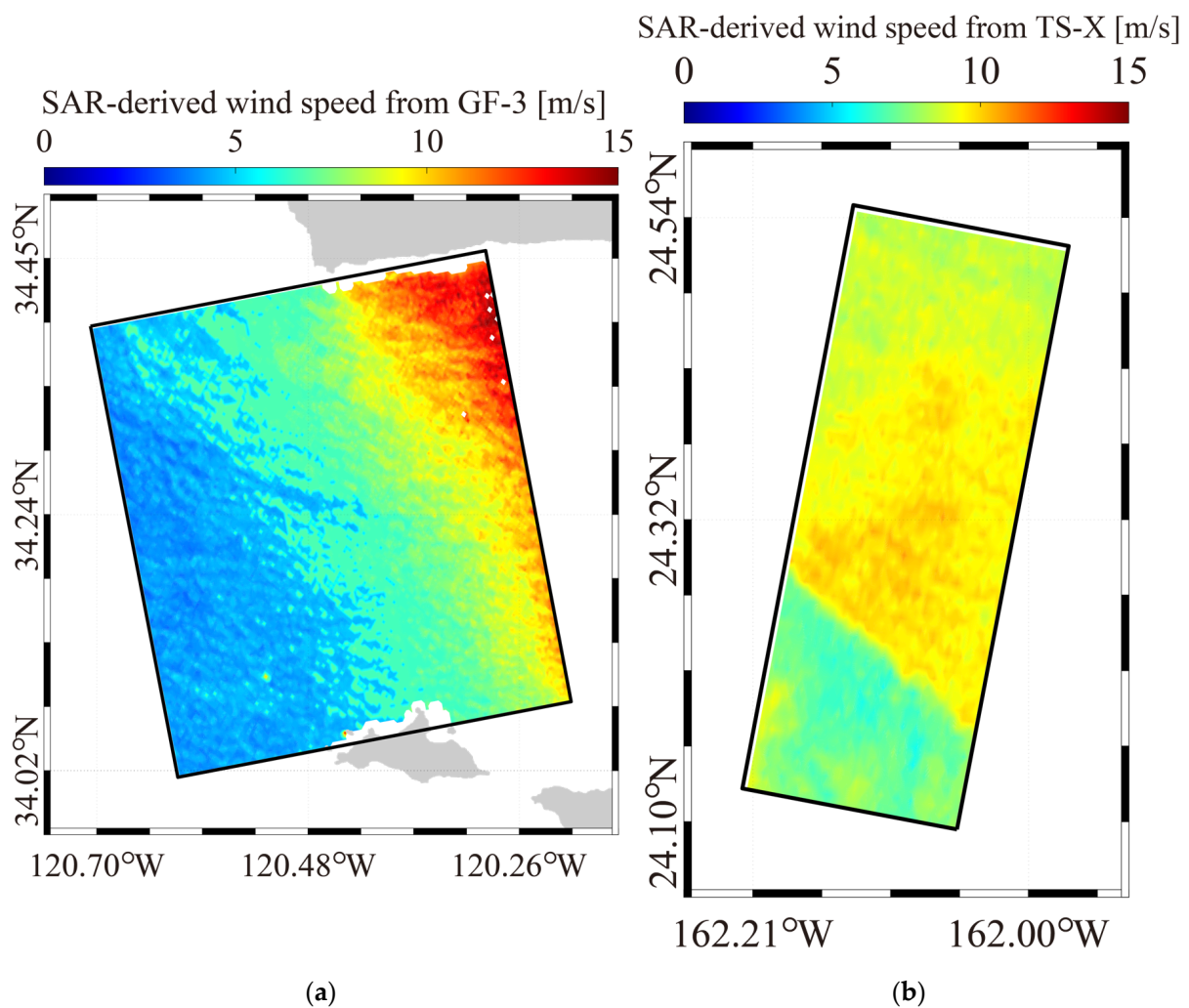


**Figure 7.** SAR-derived wind maps obtained (a) using CSARMOD-GF from the GF-3 SAR image at 1:58 UTC on 5 May 2017, and (b) using XMOD-2 from the TS-X image at 16:53 UTC on 3 August 2009.

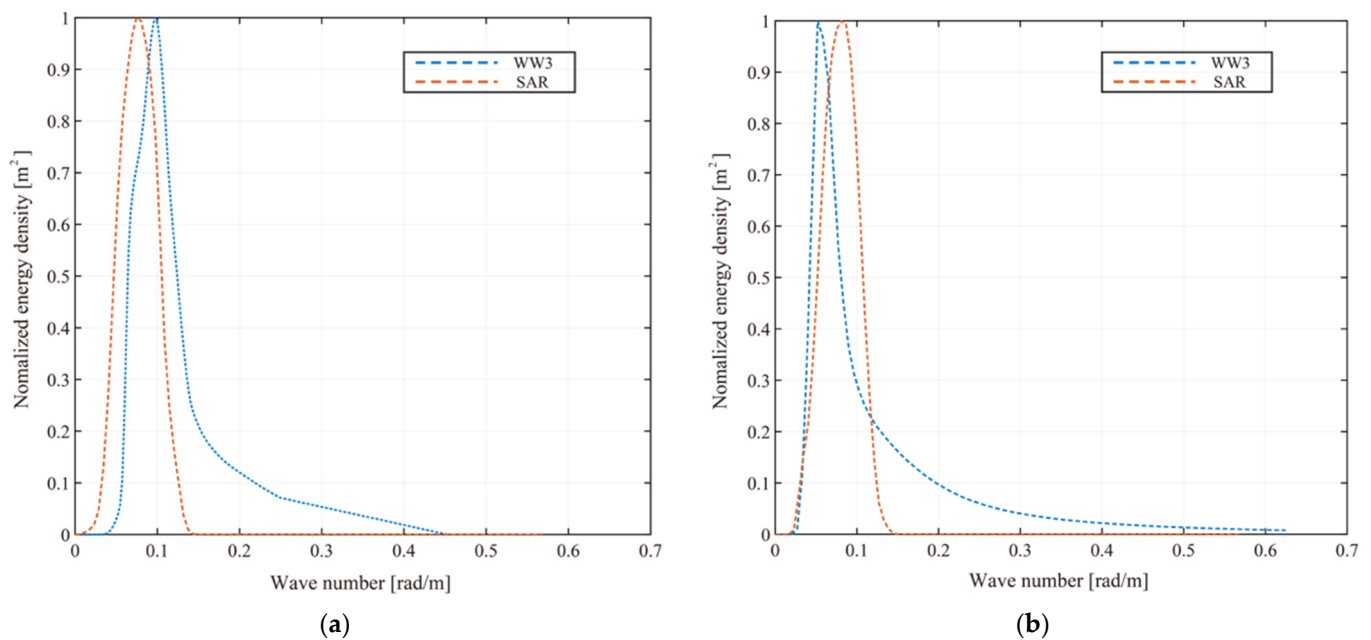


**Figure 8.** The one-dimensional wave spectra obtained using the parameterized first-guess spectrum method (PFSM) scheme: (a) results for a sub-scene of the GF-3 SAR image covering a buoyed area (ID: 46054); and (b) results for a sub-scene on the TS-X image covering a buoyed area (ID: 51001).

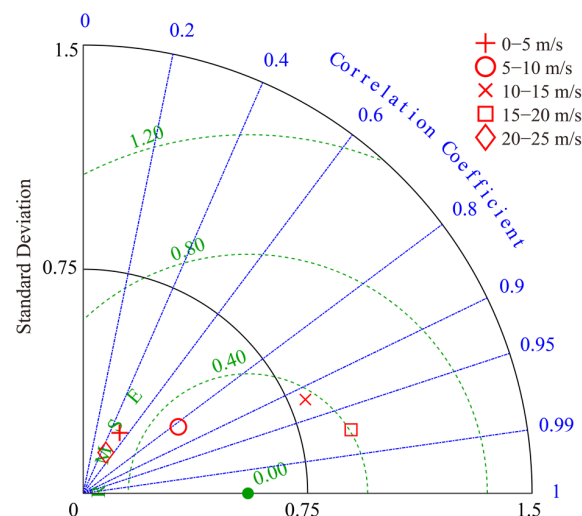


**Figure 9.** Validation of SAR-derived SWH against simulation results of the WW3 model in terms of wind speeds between 0 and 25 m/s.

#### 4.2. NP Contribution in Dual-Polarized C-Band and X-Band SAR

The predicted NRCS was composited using the Bragg resonant component and the surface radar backscattering model and the N-P contribution was estimated from the dual-polarized SAR image. The simulated NRCS maps corresponding to the GF-3 image acquired at 01:58 UTC on 5 May 2017 and the TS-X image acquired at 16:53 UTC on 3 August 2009 are shown in Figure 10a,b, respectively. Although the simulated and measured NRCSs have the same spatial structure, there are obvious differences in the NRCSs, especially for the GF-3 SAR image. It is necessary to figure out that the singular values of the simulated NRCS for the GF-3 image are caused by the invalid Bragg resonant components, indicating that the radar backscattering model needs to be further improved.

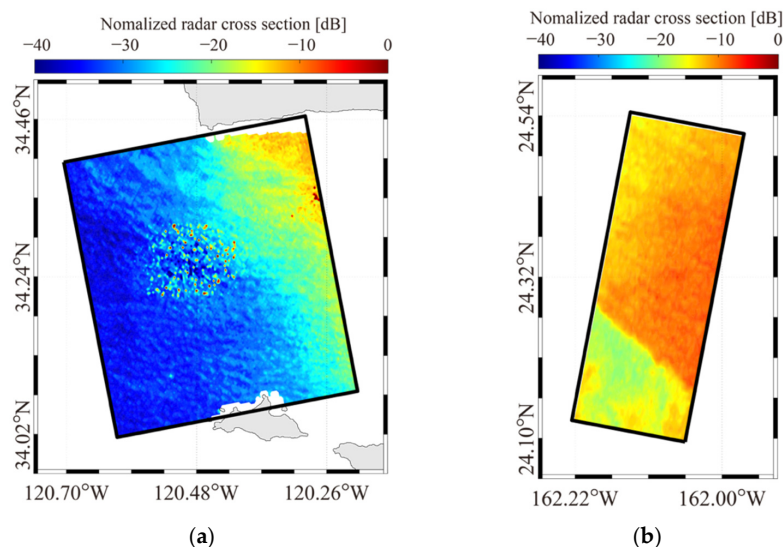


**Figure 10.** The composited NRCS map, including the Bragg resonant and N-P contribution: (a) GF-3 image acquired at 01:58 UTC on 5 May 2017; (b) TS-X image acquired at 16:53 UTC on 3 August 2009.

The composited NRCSs were compared with the observations of the GF-3 and TS-X images. Figure 11 shows the Taylor diagram analysis in terms of the SAR-derived wind speed. The RMSE of the NRCS is less than 3 dB at low-to-moderate wind speeds (<15 m/s), and the RMSE is reduced to about 6 dB at wind speeds of >20 m/s. The SAR-derived wind speeds were used to produce the wave spectrum using the JONSWAP model, which works well for the wind-sea spectrum. The relatively low accuracy of the simulated NRCS is probably due to two reasons: the transitive error of the SAR-derived wind speed and the exclusion of the swell spectrum in the calculation. Therefore, the simulated NRCS at wind speeds >20 m/s was removed in the later analysis of the NP contribution.

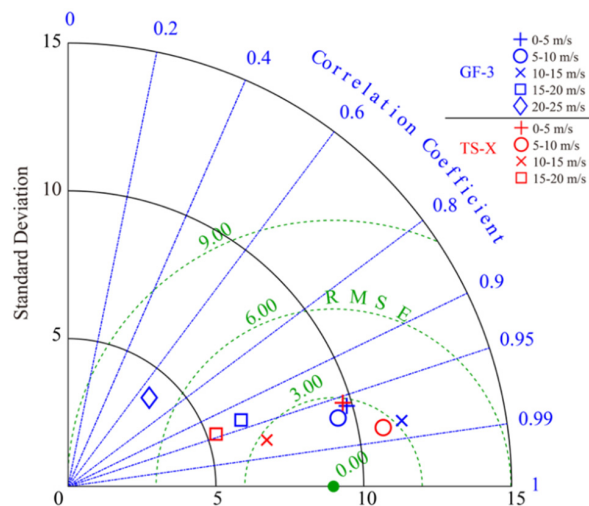


**Figure 11.** Comparison of composited NRCS with SAR-measured NRCS for wind speeds of 0 to 25 m/s. The blue and red marks illustrate the results for GF-3 and TS-X, respectively.

The ratio of the NP component  $\sigma_{wb}$  on the  $\sigma_0^{VV}$  and NRCS  $\sigma_0^{HH}$  was calculated for investigating the performance of the NP contribution to the dual-polarized C-band and X-band SAR. Figure 12 shows the relationships between the ratio ( $\sigma_{wb}/\sigma_0^{VV}$  and  $\sigma_{wb}/\sigma_0^{HH}$ ) and the SAR-derived wind speed, SAR-derived SWH, and HYCOM current speed. The red and black lines illustrate the results for the GF-3 and TS-X images, respectively. In general, the ratios for the GF-3 are higher than those of the TS-X. The wavelength (~5 cm) at C-band is longer than the ~3 cm of wavelength at the X-band. In the literature, the Bragg resonant

backscattering at X-band is higher than that at C-band, because backscattering signals are proportional to the quantity of Bragg waves. On other hand, the long waves are reduced to be capillary-gravity waves due to the energy dissipation of wave breaking. The wind-induced waves are mixed with breaking capillary gravity, indicating that NRCS at X-band  $\sigma_0^{TS-X}$  is larger than NRCS at C-band  $\sigma_0^{GF-3}$  in the background of wave breaking. That is the reason the backscattering signal in the C-band is likely sensitive to wave breaking. Moreover, the ratios are slightly greater in HH-polarization than in VV-polarization, which is consistent with the results of a previous study [36]. As can be seen from Figure 1a,b, the VV-polarized and HH-polarized ratios are small (<0.3) at low wind speeds (<4 m/s), and the ratio for GF-3 is about 0.1 larger than the ratio for TS-X. The ratio significantly increases at low-to-moderate wind speeds (<20 m/s), indicating that the NP component  $\sigma_{wb}$  can be conveniently estimated using wind speed. However, it was found that the ratio reaches 0.8 at a wind speed of 20 m/s. We believe that this behavior was caused by the smaller amount of data for high wind speeds, and it needs to be further studied in tropical cyclones. The relationships between the ratio and the SAR-derived SWH and HYCOM current are exhibited in Figure 12b,c,e,f, from which it is difficult to draw conclusions.

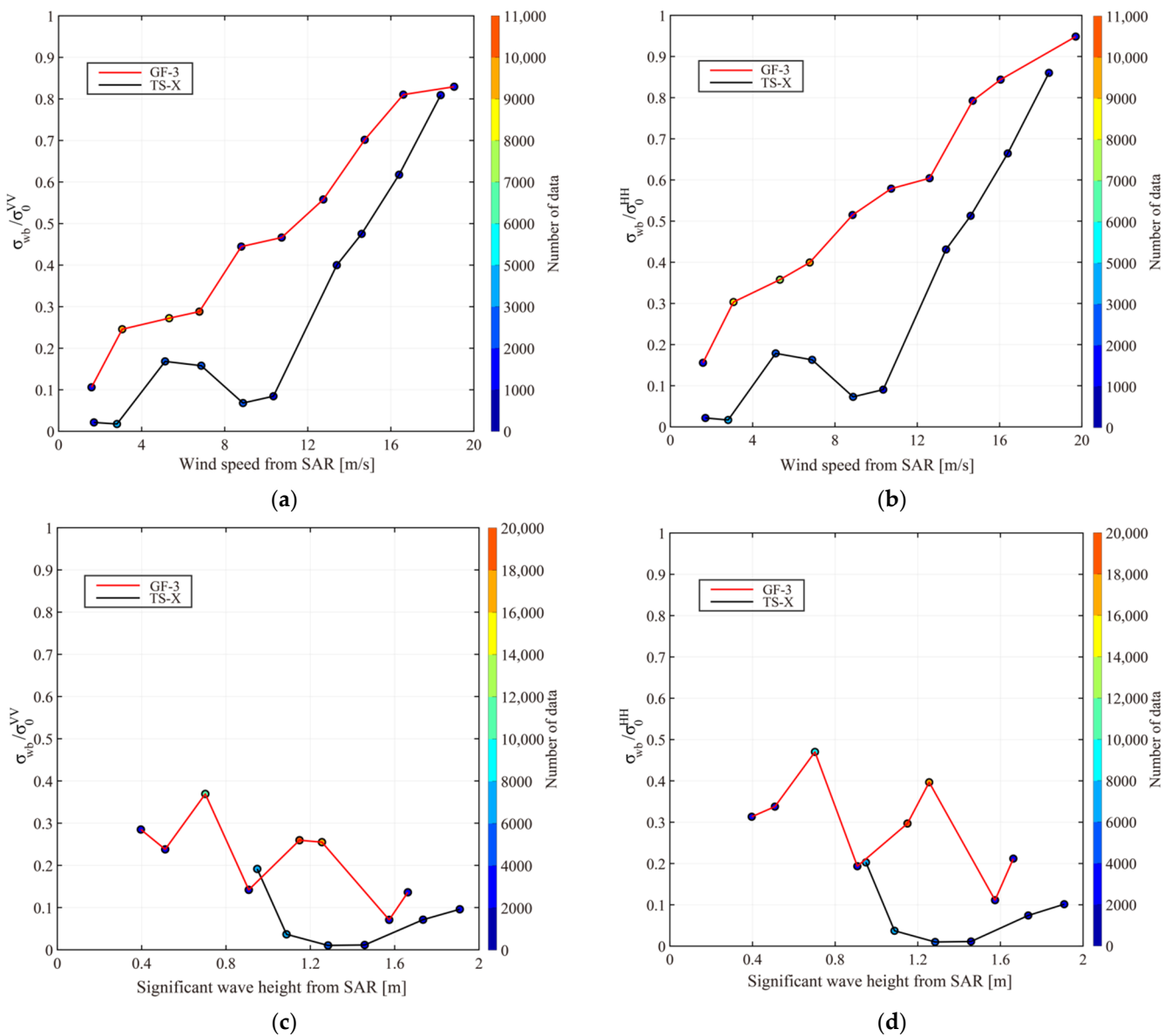
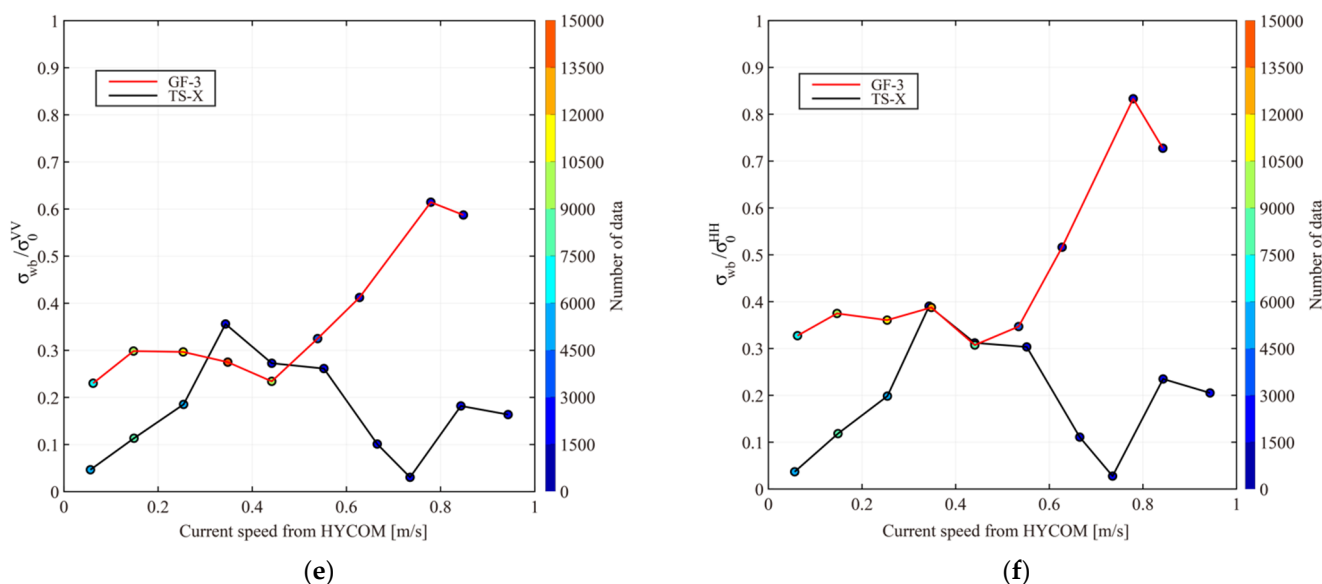


Figure 12. Cont.



**Figure 12.** The relations between the ratio ( $\sigma_{wb}/\sigma_0^{VV}$  and  $\sigma_{wb}/\sigma_0^{HH}$ ) and the (a,b) SAR-derived wind speed, (c,d) SAR-derived SWH, and (e,f) HYCOM current speed. The blue and red marks illustrate the results for GF-3 and TS-X, respectively.

4.3. Discussion

To better understand the influence of wave breaking on the SAR wave retrieval, the bias (SAR-derived SWH minus WW3-simulated results) was evaluated with respect to the whitecap coverage that is simulated by the WW3 model, as exhibited in Figure 13. It was found that the bias decreased for whitecap coverages of smaller than 0.005 and then increased with increasing whitecap coverage. The typical accuracy of the SAR-derived SWH was about 0.5 m. The variation in the bias also indicated that the bias increased with increasing wind speed. In particular, the bias was greater than  $-0.5$  m when the wind speed was greater than 18 m/s. This behavior is supposedly strong in tropical cyclones due to the occurrence of extreme winds. Under this circumstance, the improvement of the SAR wave retrieval algorithm should take into account the effect of wave breaking, although this study only gives one inference.

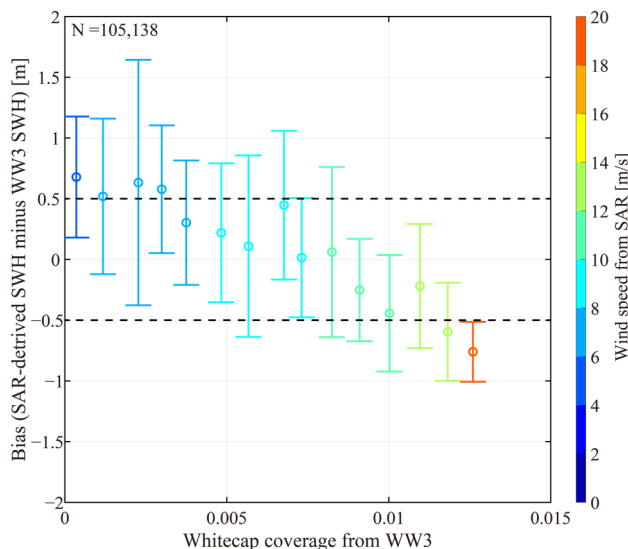


**Figure 13.** Validation of the SAR-derived SWH against the simulation results of the WW3 model in terms of the whitecap coverage from the WW3 model. The color bar denotes the SAR-derived wind speed.

## 5. Conclusions

Wave breaking is a normal marine phenomenon in open sea areas and coastal waters. Due to its advantages of an all-weather capability and fine spatial resolution, SAR is an advanced remote-sensed technique for small- and meso-scale marine dynamics detection, especially for monitoring breaking waves. Most research is tailored to the development of SAR wind and wave retrieval algorithms since the 1990s. NP caused by wave breaking at small scales is an important aspect of SAR due to the non-Bragg backscattering. In this sense, it is necessary to analyze the performance of wave breaking on C-band and X-band SAR at various sea states and forward study its effect on wave retrieval.

In total, 190 SAR images were collected, including 140 GF-3 images acquired in QPS mode and 50 dual-polarized (VV and HH) TS-X images acquired in SM mode. These images were collocated with the waves simulated by the WW3 model and the current from HYCOM. The WW3-simulated SWH and the whitecap coverage were compared with ERA-5 SWH data and measurements from NDBC buoys, respectively, yielding an RMSE of about 0.2 m for SWHs of 0–4 m and RMSEs of 0.1–0.3 for the whitecap coverage at wind speeds of 0–18 m/s. Utilizing the SAR-derived wind, WW3-simulated wave parameters, and HYCOM current, the Bragg resonant roughness was calculated with the theoretical backscattering model. Subsequently, the polarization ratio between the VV-polarized and HH-polarized resonant components of the Bragg backscattering was calculated. Finally, the NP component in the NRCS  $\sigma_{wb}$  was estimated using the SAR-measured NRCS in both the VV-polarization  $\sigma_0^{VV}$  and HH-polarization  $\sigma_0^{HH}$  channels and the polarization ratio. The sum of the Bragg and NP components in the NRCS was compared with the SAR-measured NRCS, yielding an RMSE of <3 dB at low-to-moderate wind speeds (<15 m/s); however, the accuracy decreased to 6 dB at a wind speed of about 20 m/s.

The variations in the ratio ( $\sigma_{wb}/\sigma_0^{VV}$  and  $\sigma_{wb}/\sigma_0^{HH}$ ) with respect to the SAR-derived wind, SAR-derived SWH, and HYCOM current were analyzed. In terms of the wind speed, it was found that the backscattering signal in the C-band was more sensitive than the backscattering signal in the X-band, and the ratio for GF-3 was about 0.1 higher than the ratio for TS-X. However, the ratios have less relation with the SWH and current. The variations in the bias (SAR-derived SWH minus WW3 simulation) decreased at whitecap coverages of <0.005 and then increased with increasing whitecap coverage. Moreover, the bias increased for wind speeds of >8 m/s and the bias was greater than 0.5 m at wind speeds of greater than 18 m/s, indicating that wave breaking distorts the SAR wave retrieval under strong winds, such as typhoons and hurricanes.

In our previous studies, strong wind retrieval was performed from Sentinel-1 [50] and TS-X [51] images for several tropical cyclones, creating an opportunity for further investigation of the NP contribution and improving the SAR wave retrieval algorithm under extreme sea states.

**Author Contributions:** Conceptualization, W.S. and R.Z.; methodology, W.S. and X.J.; validation, R.Z. and C.Z.; formal analysis, W.S., X.J. and J.Z.; investigation, W.S. and R.Z.; resources, W.S.; writing—original draft preparation, W.S., C.Z. and J.Z.; writing—review and editing, W.S. and R.Z.; visualization, R.Z.; funding acquisition, W.S. All authors have read and agreed to the published version of the manuscript.

**Funding:** This research was funded by the National Natural Science Foundation of China (grant numbers 42076238, 42176012, and 42130402), Shanghai University Student Innovation and Entrepreneurship Training Program (grant number S202210264031) and the Shanghai Frontiers Research Center of the Hadal Biosphere.

**Institutional Review Board Statement:** Not applicable.

**Informed Consent Statement:** Not applicable.

**Data Availability Statement:** Not applicable.

**Acknowledgments:** Gaofen-3 (GF-3) SAR images were provided by the National Ocean Satellite Application Center (NSOAS) via <https://osdds.nsoas.org.cn> (accessed on 1 January 2023). TerraSAR-

X (TS-X) images were acquired from the science AOs OCE2995 and OCE3150 provided by the German Aerospace Center (DLR). The European Centre for Medium-Range Weather Forecasts (ECMWF) data were accessed at <http://www.ecmwf.int> (accessed on 1 January 2023). The sea surface current data from the HYbrid Coordinate Ocean Model (HYCOM) were obtained from <https://www.hycom.org> (accessed on 1 January 2023). The measurements from the National Data Buoy Center (NDBC) were obtained from <http://www.ndbc.noaa.gov> (accessed on 1 January 2023). The General Bathymetric Chart of the Oceans (GEBCO) data were downloaded from <ftp.edcftp.cr.usgs.gov> (accessed on 1 January 2023). The source code for the WAVEWATCH-III (WW3) model was kindly supplied by the National Centers for Environmental Prediction (NCEP) of the National Oceanic and Atmospheric Administration (NOAA).

**Conflicts of Interest:** The authors declare that there are no conflict of interest. The funders had no role in the design of the study; in the collection, analyses, and interpretation of the data; in the writing of the manuscript; or in the decision to publish the results.

## Appendix A

**Table A1.** Settings of the WAVEWATCH-III model (WW3) (version 6.07).

Forcing field	European Centre for Medium-Range Weather Forecasts (ECMWF) reanalysis data at a 0.25° grid and a time interval of 1-h sea surface current data from HYbrid Coordinate Ocean Model (HYCOM) at a spatial resolution of 0.08° grid and a time interval of 3-h; and water depth data from the General Bathymetric Chart of the Oceans (GEBCO) having a spatial resolution of 0.01° grid
Other settings	The bins ranged logarithmically between 0.04118 and 0.7186 at an interval of $\Delta f/f = 0.1$ . The spatial propagation was characterized by 300 s time steps in both the longitudinal and latitudinal directions.
Resolution	Significant wave height having at a 0.05° grid and temporal resolution of 30-min and the wave spectrum resolved into 24 regular azimuthal directions at a step of 15°.
Parameterizations	The input/dissipation terms using switches ST2 and STAB2; the wave-wave interactions using the switch GMD

## Appendix B

In the literature, the whitecap coverage from the National Data Buoy Center (NDBC) buoys is calculated as follows [52]:

$$W = 2.98 \times 10^{-5} R_B^{4.04}, \quad (\text{A1})$$

where

$$R_B = (g\nu)^{-1} u_*^3 \beta, \quad (\text{A2})$$

$$\beta = \frac{g}{\omega_p u_*} \quad (\text{A3})$$

$$u_* = \sqrt{C_d U_{10}^2} \quad (\text{A4})$$

In Equations (A1)–(A4),  $W$  is the whitecap coverage;  $R_B$  is the wave breaking parameter;  $g = 9.8 \text{ m/s}^2$ ;  $\nu$  is the kinematic viscosity of air;  $u_*$  is the air friction velocity;  $C_d$  is the drag coefficient;  $U_{10}$  is the drag coefficient;  $\beta$  is the wave age; and  $\omega_p$  is the peak angular frequency of the wind-wave. Therefore, the whitecap coverage is conveniently calculated when the wind and wave parameters are known.



## References

1. Melville, K. The role of surface-wave breaking in air-sea interaction. *Annu. Rev. Fluid. Mech.* **1996**, *28*, 279–321. [[CrossRef](#)]
2. Sun, Z.F.; Shao, W.Z.; Yu, W.P.; Li, J. A study of wave-induced effects on sea surface temperature simulations during typhoon events. *J. Mar. Sci. Eng.* **2021**, *9*, 622. [[CrossRef](#)]
3. Sun, Z.F.; Shao, W.Z.; Wang, W.L.; Zhou, W.; Yu, W.P.; Shen, W. Analysis of wave-induced Stokes transport effects on sea surface temperature simulations in the Western Pacific Ocean. *J. Mar. Sci. Eng.* **2021**, *9*, 834. [[CrossRef](#)]
4. Isaksen, L.; Stoffelen, A. ERS scatterometer wind data impact on ECMWF's tropical cyclone forecasts. *IEEE Trans. Geosci. Electron.* **2000**, *38*, 1885–1892. [[CrossRef](#)]
5. Stoffelen, A.; Anderson, T. Wind retrieval and ERS-1 scatterometer radar backscatter measurements. *Adv. Space Res.* **1993**, *13*, 53–60. [[CrossRef](#)]
6. Lemoine, F.G.; Zelensky, N.P.; Chinn, D.S.; Pavlis, D.E.; Rowlands, D.D.; Beckley, B.; Luthcke, S.B.; Willis, P.; Ziebart, M.; Luceri, V. Towards development of a consistent orbit series for TOPEX, Jason-1, and Jason-2. *Adv. Space Res.* **2010**, *46*, 1513–1540. [[CrossRef](#)]
7. Hersbach, H. Comparison of C-band scatterometer CMOD5.N equivalent neutral winds with ECMWF. *J. Atmos. Ocean. Technol.* **2010**, *27*, 721–736. [[CrossRef](#)]
8. Shao, W.Z.; Nunziata, F.; Zhang, Y.G.; Corcione, V.; Migliaccio, M. Wind speed retrieval from the Gaofen-3 synthetic aperture radar for VV- and HH-polarization using a re-tuned algorithm. *Eur. J. Remote Sens.* **2021**, *54*, 318–337. [[CrossRef](#)]
9. Shao, W.Z.; Zhang, Z.; Li, X.M.; Wang, W.L. Sea surface wind speed retrieval from TerraSAR-X HH polarization data using an improved polarization ratio model. *IEEE J. Sel. Top. Appl. Earth. Obs. Remote Sens.* **2016**, *9*, 4991–4997. [[CrossRef](#)]
10. Chapron, B.; Johnsen, H.; Garello, R. Wave and wind retrieval from SAR images of the ocean. *Ann. Intern. Med.* **2001**, *56*, 682–699. [[CrossRef](#)]
11. Monaldo, M. Comparison of SAR-derived wind speed with model predictions and ocean buoy measurements. *IEEE Trans. Geosci. Remote Sens.* **2001**, *39*, 2587–2600. [[CrossRef](#)]
12. Li, X.M.; Lehner, S. Algorithm for sea surface wind retrieval from TerraSAR-X and TanDEM-X data. *IEEE Trans. Geosci. Remote Sens.* **2014**, *52*, 2928–2939. [[CrossRef](#)]
13. Shimada, T.; Kawamura, H. An L-band geophysical model function for SAR wind retrieval using JERS-1 SAR. *IEEE Trans. Geosci. Remote Sens.* **2003**, *41*, 518–531. [[CrossRef](#)]
14. Yang, X.F.; Li, X.F.; Zheng, Q.A.; Gu, X.F.; Pichel, W.G.; Li, Z.W. Comparison of ocean-surface winds retrieved from QuikSCAT scatterometer and Radarsat-1 SAR in offshore waters of the U.S. west coast. *IEEE Geosci. Remote Sens. Lett.* **2011**, *8*, 163–167. [[CrossRef](#)]
15. Yao, R.; Shao, W.Z.; Jiang, X.W.; Yu, T. Wind speed retrieval from Chinese Gaofen-3 synthetic aperture radar using an analytical approach in the nearshore waters of China's seas. *Int. J. Remote Sens.* **2022**, *43*, 3028–3048. [[CrossRef](#)]
16. Shao, W.Z.; Sheng, Y.X.; Sun, J. Preliminary assessment of wind and wave retrieval from Chinese Gaofen-3 SAR imagery. *Sensors* **2017**, *17*, 1705. [[CrossRef](#)]
17. Hwang, A.; Zhang, B.; Toporkov, V.; Perrie, W. Comparison of composite Bragg theory and quad-polarization radar backscatter from RADARSAT-2: With applications to wave breaking and high wind retrieval. *J. Geophys. Res. Oceans* **2010**, *115*, C08019. [[CrossRef](#)]
18. Zhang, B.; Perrie, W. Cross-Polarized Synthetic Aperture Radar: A new potential measurement technique for hurricanes. *Bull. Am. Meteorol. Soc.* **2012**, *93*, 531–541. [[CrossRef](#)]
19. Shao, W.Z.; Yuan, X.Z.; Sheng, Y.X.; Sun, J.; Zhou, W.; Zhang, Q.J. Development of wind speed retrieval from cross-polarization Chinese Gaofen-3 synthetic aperture radar in typhoons. *Sensors* **2018**, *18*, 412. [[CrossRef](#)]
20. Engen, G.; Vachon, P.W.; Johnsen, H.; Dobson, F.W. Retrieval of ocean wave spectra and RAR MTF's from dual-polarization SAR data. *IEEE Trans. Geosci. Remote Sens.* **2000**, *38*, 391–403. [[CrossRef](#)]
21. Dankert, H.; Horstmann, J. Detection of wave groups in SAR images and radar image sequences. *IEEE Trans. Geosci. Remote Sens.* **2003**, *41*, 1437–1446. [[CrossRef](#)]
22. Alpers, R.; Bruening, C. On the relative importance of motion-related contributions to the SAR Imaging mechanism of ocean surface waves. *IEEE Trans. Geosci. Remote Sens.* **1986**, *GE-24*, 873–885. [[CrossRef](#)]
23. Alpers, R.; Ross, B.; Rufenach, L. On the detectability of ocean surface waves by real and synthetic aperture radar. *J. Geophys. Res. Oceans* **1981**, *86*, 6481. [[CrossRef](#)]
24. Hasselmann, K.; Hasselmann, S. On the nonlinear mapping of an ocean wave spectrum into a synthetic aperture radar image spectrum and its inversion. *J. Geophys. Res. Oceans* **1991**, *96*, 10713. [[CrossRef](#)]
25. Mastenbroek, C.; Valk, C. A semiparametric algorithm to retrieve ocean wave spectra from synthetic aperture radar. *J. Geophys. Res. Oceans* **2000**, *105*, 3497–3516. [[CrossRef](#)]
26. Schulz-Stellenfleth, J.; Lehner, S.; Hoja, D. A parametric scheme for the retrieval of two-dimensional ocean wave spectra from synthetic aperture radar look cross spectra. *J. Geophys. Res. Oceans* **2005**, *110*, C05004. [[CrossRef](#)]
27. Shao, W.Z.; Jiang, X.W.; Sun, Z.F.; Hu, Y.Y.; Marino, A.; Zhang, Y.G. Evaluation of wave retrieval for Chinese Gaofen-3 synthetic aperture radar. *Geo-Spat. Inf. Sci.* **2022**, *25*, 229–243. [[CrossRef](#)]
28. Stopa, E.; Mouche, A. Significant wave heights from Sentinel-1 SAR: Validation and applications. *J. Geophys. Res. Oceans* **2017**, *122*, 1827–1848. [[CrossRef](#)]

29. Pleskachevsky, L.; Rosenthal, W.; Lehner, S. Meteo-marine parameters for highly variable environment in coastal regions from satellite radar images. *ISPRS J. Photogramm. Remote Sens.* **2016**, *119*, 464–484. [[CrossRef](#)]
30. Pleskachevsky, A.; Jacobsen, S.; Tings, B.; Schwarz, E. Estimation of sea state from Sentinel-1 Synthetic aperture radar imagery for maritime situation awareness. *Int. J. Remote Sens.* **2019**, *40*, 4104–4142. [[CrossRef](#)]
31. Alpers, W.; Brümmer, B. Atmospheric boundary layer rolls observed by the synthetic aperture radar aboard the ERS-1 satellite. *J. Geophys. Res. Oceans* **1994**, *99*, 12613. [[CrossRef](#)]
32. Zhang, L.; Shi, H.; Du, H.; Chen, X. Estimation of sea surface wind direction using spaceborne SAR images and wavelet analysis. *J. Remote Sens.* **2014**, *18*, 215–230. [[CrossRef](#)]
33. Kudryavtsev, V.N.; Chapron, B.; Myasoedov, A.G.; Collard, F.; Johannessen, J.A. On dual co-polarized SAR measurements of the ocean surface. *IEEE Geosci. Remote Sens. Lett.* **2013**, *10*, 761–765. [[CrossRef](#)]
34. Kudryavtsev, V.; Kozlov, I.; Chapron, B.; Johannessen, J.A. Quad-polarization SAR features of ocean currents. *J. Geophys. Res. Oceans* **2014**, *119*, 6046–6065. [[CrossRef](#)]
35. Kudryavtsev, V.; Fan, S.; Zhang, B.; Mouche, A.; Chapron, B. On quad-polarized SAR measurements of the ocean surface. *IEEE Trans. Geosci. Remote Sens.* **2019**, *57*, 8362–8370. [[CrossRef](#)]
36. Sun, Z.F.; Shao, W.Z.; Jiang, X.W.; Nunziata, F.; Wang, W.L.; Shen, W.; Migliaccio, M. Contribution of breaking wave on the co-polarized backscattering measured by the Chinese Gaofen-3 SAR. *Int. J. Remote Sens.* **2022**, *43*, 1384–1408. [[CrossRef](#)]
37. Viana, R.; Lorenzetti, J.; Carvalho, J.; Nunziata, F. Estimating energy dissipation rate from breaking waves using polarimetric SAR images. *Sensors* **2020**, *20*, 6540. [[CrossRef](#)]
38. Hu, Y.Y.; Shao, W.Z.; Shi, J.; Sun, J.; Ji, Q.Y.; Cai, L.N. Analysis of the typhoon wave distribution simulated in WAVEWATCH- III model in the context of Kuroshio and wind-induced current. *J. Oceanol. Limnol.* **2020**, *38*, 1692–1710. [[CrossRef](#)]
39. Plant, J. A stochastic, multiscale model of microwave backscatter from the ocean. *J. Geophys. Res.* **2002**, *107*, 3120. [[CrossRef](#)]
40. Xie, T.; Zhao, S.Z.; Perrie, W.; Fang, H.; Yu, W.J.; He, Y.J. Electromagnetic backscattering from one-dimensional drifting fractal sea surface I: Wave–current coupled model. *Chin. Phys. B* **2016**, *25*, 064101. [[CrossRef](#)]
41. Kudryavtsev, S.; Hauser, D.; Caudal, G.; Chapron, B. A semiempirical model of the normalized radar cross-section of the sea surface 1. Background model. *J. Geophys. Res.* **2003**, *108*, FET21–FET224. [[CrossRef](#)]
42. Phillips, M. Spectral and statistical properties of the equilibrium range in wind-generated gravity waves. *J. Fluid. Mech.* **1985**, *156*, 505. [[CrossRef](#)]
43. Pierson, J.; Moskowitz, L. A proposed spectral form for fully developed wind seas based on the similarity theory of S. A. Kitaigorodskii. *J. Geophys. Res. Planets* **1964**, *69*, 5181–5190. [[CrossRef](#)]
44. Romeiser, R.; Alpers, W.; Wismann, V. An improved composite surface model for the radar backscattering cross section of the ocean surface: 1. Theory of the model and optimization/validation by scatterometer data. *J. Geophys. Res. Oceans* **1997**, *102*, 25237–25250. [[CrossRef](#)]
45. Elfouhaily, T.; Chapron, B.; Katsaros, K.; Vandemark, D. A unified directional spectrum for long and short wind-driven waves. *J. Geophys. Res. Oceans* **1997**, *102*, 15781–15796. [[CrossRef](#)]
46. Hasselmann, E.; Duncel, M.; Ewing, A. Directional wave spectra observed during JONSWAP 1973. *J. Phys. Oceanogr.* **1980**, *10*, 1264–1280. [[CrossRef](#)]
47. Shao, W.Z.; Li, X.F.; Sun, J. Ocean wave parameters retrieval from TerraSAR-X images validated against buoy measurements and model results. *Remote Sens.* **2015**, *7*, 12815–12828. [[CrossRef](#)]
48. Zhu, S.; Shao, W.Z.; Armando, M.; Shi, J.; Sun, J.; Yuan, X.Z.; Hu, J.C.; Yang, D.K.; Zuo, J.C. Evaluation of Chinese quad-polarization Gaofen-3 SAR wave mode data for significant wave height retrieval. *Can. J. Remote Sens.* **2019**, *44*, 588–600. [[CrossRef](#)]
49. Sun, J.; Guan, C.L. Parameterized first-guess spectrum method for retrieving directional spectrum of swell-dominated waves and huge waves from SAR images. *Chin. J. Oceanol. Limn.* **2006**, *24*, 12–20. [[CrossRef](#)]
50. Shao, W.; Lai, Z.; Nunziata, F.; Buono, A.; Jiang, X.; Zuo, J. Wind field retrieval with rain correction from dual-polarized Sentinel-1 SAR imagery collected during tropical cyclones. *Remote Sens.* **2022**, *14*, 5006. [[CrossRef](#)]
51. Shao, W.; Hu, Y.; Nunziata, F.; Corcione, V.; Migliaccio, M.; Li, X. Cyclone wind retrieval based on X-band SAR-derived wave parameter estimation. *J. Atmos. Ocean. Technol.* **2020**, *37*, 1907–1924. [[CrossRef](#)]
52. Zhao, D.L.; Toba, Y. Dependence of whitecap coverage on wind and wind-wave properties. *J. Oceanogr.* **2001**, *57*, 603–616. [[CrossRef](#)]

**Disclaimer/Publisher’s Note:** The statements, opinions and data contained in all publications are solely those of the individual author(s) and contributor(s) and not of MDPI and/or the editor(s). MDPI and/or the editor(s) disclaim responsibility for any injury to people or property resulting from any ideas, methods, instructions or products referred to in the content.